Colloid Polym Sci 277:914–930 (1999)

ORIGINAL CONTRIBUTION

C.D. Dushkin
G.S. Lazarov
S.N. Kotsev
H. Yoshimura
K. Nagayama

Effect of growth conditions on the structure of two-dimensional latex crystals: experiment

Received: 8 February 1999
Accepted in revised form: 12 May 1999

C.D. Dushkin (✉)
Mitsubishi Chemical Corporation
Yokohama Research Center
Non-Equilibrium Laboratory
1000 Kamoshida-cho, Aoba-ku
Yokohama 227-8502, Japan
e-mail: dushkin@atlas.rc.m-kagaku.co.jp

G.S. Lazarov · S.N. Kotsev
Temple University
Department of Physics, Barton Hall,
Room A116
Philadelphia, PA 19122, USA

H. Yoshimura
Meiji University, Department of Physics
School of Science and Technology
1-1-1 Higashi-mita, Tama-ku
Kawasaki 214-71, Japan

K. Nagayama
National Institute of Physiological Science
Department of Molecular Physiology
Myodaiji-cho, Okazaki 444, Japan

Abstract The growth kinetics and structure of two-dimensional crystals of fine latex particles on solid substrates have been studied using a variety of microscopic techniques: optical microscopy, surface plasmon resonance microscopy, transmission electron microscopy, scanning electron microscopy and atomic force microscopy. A circular-shaped crystal is grown from a thin layer of a latex suspension by a two-step mechanism: nucleation and crystal growth. Here we report an experimental study of the factors influencing the crystallization process, especially focusing on the water evaporation rate, the liquid meniscus at the crystal boundary, the particle size and concentration, the substrate, etc. Crystals of good quality and structure are grown at a high evaporation rate (low humidity) favoring a convection-dominated influx of particles from the suspension. The particle diffusion plays a role at suppressed evaporation thus causing an increase in the number of crystal defects. The dynamics of the meniscus slope leads to growth instability resulting in a sequence of multilayer rings. A hexagonal lattice prevails in the final crystal whereas a square lattice is observed in the transition regions between two different hexagonal multilayers. These general trends of the crystallization process are the same for different particle diameters (19 nm, 55 nm, 144 nm and 1.696 μm), volume fractions (0.001–0.01) and substrates (bare and metal-coated glass and mica).

Key words Two-dimensional crystal · Kinetics of crystal growth · Growth instability · Surface plasmon resonance · Crystal defect

Introduction

Classically, a crystal is considered to be a uniform array of ordered atoms or molecules "constructed by the infinite repetition of identical structural units in space" [1]. A bulk crystal results from the repetition of 1 of 14 3D lattice types of different geometry. Here one should also refer to protein crystals composed of macromolecules with intrinsic symmetry, which increases the variety of crystal forms [2]. 3D colloidal crystals have as their elements various fine particles of submicron size with latex spheres as the most common representatives. At the same time, 2D lattice types can also be considered: square, hexagonal, etc. [1]. If for simple atoms and molecules of high reaction affinity they are less probable at ambient conditions, well-defined 2D crystalline lattices can be observed in thin particle layers of proteins [3], latexes (see below) and even millimeter-sized objects such as gas bubbles [4] and topologically matched species [5]. Intuitively, a 2D crystal has one of its dimensions, thickness, much smaller than the other two dimensions, which introduces a peculiarity in its structure and properties. Increasing the thickness from a single layer (monolayer) to a vast number of successive layers should lead to a smooth transition from a 2D to a 3D crystal.

Although fewer lattice types can be constructed due to the simplicity of a spherical particle, latex crystals can model the general features of the crystalline state not visible for atomic and molecular crystals [6]. There are two types of crystalline assembly of latex particles representing research and practical interest:

1. Wet crystals remain at any moment partially or completely immersed in the solvent (water) in which the particles are originally dissolved. A wet 3D crystal is formed in a latex suspension enclosed in a glass cell of overall dimension much larger than the particle diameter [6–19]. A wet 2D crystal can form in a suspension film confined between two smooth solid surfaces located close to each other, for example lower plane surface and upper concave surface [20] or two plane surfaces at a small inclination [21, 22]. The crystal fills the gap between the solid surfaces following their profile: the monolayer is in the thinnest part of the gap, and is followed by a bilayer, triple layer, etc. Structuring of latex particles in a thin suspension layer can also be induced by powerful laser irradiation [23–25]. Ordered structures of latex particles trapped at the fluid/air interface can also be formed [26–29].

2. Dry crystals are referred to as ordered latex structures free of solvent (water) [30–33]. They usually comprise dry structured layers of latex particles deposited on a solid substrate. A dry 2D crystal consists of a monolayer (a single layer of hexagonally packed particles) coexisting with particle multilayers (bilayer, triple layer, etc.), which can be counted directly by an optical or an electron microscope depending on the particle size. Such ordered 2D media are expected to find practical applications: microscopy standards and microelectronics elements [34–39]; materials for the optical storage and processing of information [40]; templates for lithography [41], semiconductor nanoparticles [42], microporous silica [43] and fluorescent particles [44]; etc.

Our study deals with dry 2D latex crystals on a solid substrate. The main problem for their technical application is how to grow a large crystalline layer (monocrystal) in a fast and reproducible way. Any feasible process should include evaporation of the water from a wetting suspension film in a way allowing layering and arrangement of the particles in a crystalline lattice. By rotating [39] or freezing [40] a drying suspension droplet, domains of good crystallinity are found, although the number of crystal layers and their structure over the entire sample area have not been reported in these initial studies. Substantial progress in spin-coating with uniform particle layers has been made after solving the complicated hydrodynamic problems accompanying the arraying process [42, 45]. A uniform thin film forms instantaneously after applying a strong centrifugal field suppressing the capillary force over the sample area.

Another approach is the control of the capillary force by maintaining a suitable meniscus shape during the growth of a latex crystal on a solid substrate [46–48], mercury [49–51] or fluorinated oil [28]. In these experiments the latex suspension is spread in crystallization cells specifically designed for shaping the liquid layer in a way such that the crystal grows in a radial direction, from the cell center to the periphery. Then the crystallization process has two distinct stages: nucleation and crystal growth. The initial nucleus is an ordered monolayer with hexagonal packing; this forms at the cell center when the suspension film thickness becomes nearly equal to the particle diameter [49]. As soon as the particles protrude from the film surface, they are subjected to an attractive force, called the immersion capillary force [52–55]; this force plays an important role in the formation of the first ordered domain(s), referred to as the nucleus. Once a nucleus is created, and as it is drying, a convective flow brings new particles from the suspension. Therefore, the crystal growth depends strongly on the evaporation rate: at a low rate (high humidity of the air) crystallization is slowed down because of a suppressed water flow. At sufficiently decreased evaporation or at condensation of water vapor, the latex layer can even be destroyed [47].

Here we aim to study the effect of the evaporation rate on the kinetics of crystal growth and on the quality of crystal structure, along with other experimental factors such as the meniscus profile at the crystal boundary, the particle size and the concentration and the type of substrate. As briefly reported in a preliminary study [48], crystals of good quality can be produced at a relatively high evaporation rate (low humidity). A more detailed picture of crystallization at suppressed evaporation is given here for when the rate of crystallization sufficiently decreases and the diffusion of particles opposing the convection disturbs the crystalline order. Also, new experimental results obtained by us for monocrystals of various latexes (19 nm, 55 nm, 144 nm and 1.696 μm) reveal the effect of the particle diameter on the growth instability leading to the formation of ring-shaped multilayers. This instability turns out to be affected also by the size, geometry and wettability of the crystallization cell. All these data serve as the background for theoretical modeling of the crystallization stages to be reported in a subsequent paper.

The elucidation of various factors on the growth kinetics and the structure of 2D crystals by this study could help in obtaining crystals of better quality. The microscopic observations can have an impact on the technical applications of large-scale deposition methods developed recently: dip [56], drag [57] and drum [58, 59] coating.

Materials and methods

Latex particles

Different sorts of polystyrene latex particles were used as the 2D crystal elements: 55 nm, 144 nm and 1.696 μm with an original concentration of 1 wt% (JSR, Japan) and 19 nm with an original concentration 6.29 wt% (IDC, USA). As seen in Table 1, the particles are quite uniform in size and bear a negative surface charge in water. Before use the original latex solution was filtered through Millipore filters of pore size 450 nm for 144-nm particles and 100 nm for 55-nm particles. To prepare working solutions the filtrate was diluted with deionized water. For spreading, the original suspension of 19-nm latex was diluted with a water solution of the nonionic surfactant Triton X-100 at a typical concentration of 5×10^{-4} M.

Crystallization cell

The crystallization cell for growing 2D crystals of fine particles is shown in Fig. 1. The cell wall is made of a paraffin block (approximate size $20 \times 10 \times 5$ mm) with a melting point of about 70 °C (Nacalai Tesque). A circular hole of diameter 2–4 mm is pierced through the block using a calibrated screwdriver and a glass rod. The supply of suspension to and the evaporation of water from the cell can be facilitated by broadening the upper side of the hole or by decreasing the block thickness to about 1 mm. The hole is sealed on the bottom of the block by a transparent plate (glass or mica), allowing optical observation of the transmitted light. The glass plate (Matsunami microcover glass, $18 \times 18 \times 0.1$ mm) was washed with chromic acid, rinsed with deionized water and wiped with a cotton paper. As proven by atomic force microscopy (AFM), the glass plate was of good flatness over the entire area with a microroughness of no more than 2 nm, which is much less than the size of the latex particles used. The glass can easily be cleaned as well as modified by coating with various materials, for example, carbon, gold or silver. The mica plate was freshly cleaved on both sides to remove scratches on the surfaces and to create a site of perfect flatness to be used for the crystallization area. Its size, typically of about a few millimeters, is limited by step lines along the atomic planes destroyed by the cleavage. Apart from the molecular flatness, the biggest advantage of mica is that one can take replicas of a crystal for study with an electron microscope. Both glass and mica allow crystals of good quality to be produced if the suspension can be uniformly spread on the substrate. To improve its wettability, a hydrophobic substrate was briefly exposed to ion sputtering. The pretreated substrate was then sealed on the paraffin wall by melting the paraffin surface around the hole using a soldering iron. It was not always possible to melt the paraffin exactly up to the edge of the hole because the melt can spread over the clean substrate. As a result, a small circular gap with an average height of about a few microns can remain between the paraffin wall and the substrate.

Table 1 Parameters of the latex spheres used to grow 2D crystals. d is the average particle diameter, Δd is the standard deviation from the average particle diameter, ρ_p is the latex particle density, n_p is the refractive index of the particle and Q_p is the surface charge of a single latex particle

d (nm)	Δd (nm)	ρ_p (g/cm^3)	n_p	Q_p (C)	Supplier
19					IDC
55	±3.6	1.065	1.565		JSR
144	±2.0	1.065	1.565		JSR
1696	±47.2	1.057	1.592	-5.67×10^{-17} [60]	JSR

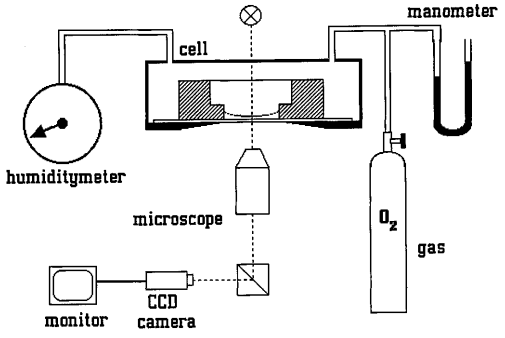

Fig. 1 Experimental setup for the growth of 2D crystals on a solid substrate. The latex suspension is dropped in the crystallization cell, which consists of a hydrophobic wall attached to a hydrophilic substrate. The crystallization cell is placed on a metal support or in a thermostated housing allowing dry gas supply

Experimental setup

The crystallization cell was placed on the translation table of an optical microscope by attaching it to a metal support (Fig. 1). It can also be enclosed in a thermostated housing made of stainless steel with a transparent cover to illuminate and isolate the cell. A few connectors mounted to the cover supply the inner space with gas and allow control measurements. The gas flows through at a pressure of about 10-mm water column. Using dry gas (nitrogen or oxygen) one can decrease the humidity sufficiently; the humidity was measured by a humidity meter operating in the range 15–100% (Sato Keiryoki). The samples were illuminated by polychromatic, green-filtered light (546 nm) or red light (632.8 nm, He-Ne laser). The observations were carried out using optical microscopes in transmitted light (Nikon) or in reflected light (Olympus). At small magnification a general view over the crystallization area was achieved, whereas at large magnification details of the crystal boundary and tracks of particles entering the crystal could be observed (even for 144-nm particles). The crystallization was recorded using a Super VHS video system.

Experimental procedures

For 55-nm and 144-nm latexes, the crystallization cell was first loaded with a 1-μl suspension droplet with a particle concentration varying between 0.05 and 1 wt% (particle volume fraction $\varphi = 0.0005$–0.001). Then the water was evaporated from the droplet at room temperature 20 °C (±2 °C). The humidity was varied over wide range: almost zero for a dry gas, about 30% in a dry air atmosphere, and about 50–70% for other conditions. Decreasing the volume of air, V_a, in contact with the suspension gradually decreases the rate of evaporation. The actual humidity, f, follows the equation

$$f = 1 - (1 - f_0)\exp(-t/\tau_e) \quad . \tag{1}$$

Here $\tau_e = V_a/\alpha kTA_e$ is the characteristic time of evaporation, f_0 is the initial room humidity (before closing the latex suspension in the cell), $k = 1.38 \times 10^{-16}$ erg/K is the Boltzmann constant, T is the absolute temperature and A_e is the surface area of evaporation. The constant α is given by $\alpha = j_{e0}/p_s(1 - f_0)$, where j_{e0} is the evaporation rate and $p_s(T)$ is the saturation pressure.

To obtain j_{e0} and α we measured the weight of an evaporating water droplet as a function of time. The initial droplet volume, V_0, was chosen to correspond to the suspension volume most frequently used in the crystallization. To be closer to reality, the

evaporating droplet was weighed as it is in the paraffin crystallization cell. The experimental data for the droplet volume $V(t)$ shown in Fig. 2 obey the equation

$$V = V_0 - w_w A_e j_{e0} t \ , \quad (2)$$

where $w_w = 3 \times 10^{-23}$ cm^3 is the volume of a water molecule. Hence, the rate of water evaporation turns out to be $j_{e0} = 6.12 \times 10^{17}$ cm^{-2} s^{-1} and $\alpha = 3.59 \times 10^{13}$ dyn^{-1} s^{-1} ($p_s = 23368$ dyn/cm^2, $T = 293$ K, $A_e = 3.14$ mm^2).

The process of crystal growth was recorded by the video system under various experimental conditions (evaporation rate, substrate and particle concentration). The latex crystal shape did not have a simple geometry throughout the growth: nearly elliptical or circular. Therefore, the crystal area, A, was measured from the records as a function of time using an image analyzer (Zeiss Videoplan 2).

Very thin layers of 19-nm latex particles were formed in a paraffin cell attached by epoxy resin (Bison) to a silver-coated glass plate. The crystal layers, hardly seen using the optical microscope, were monitored by surface plasmon resonance (SPR) microscopy [61].

The crystals of micron-sized latex, 1.696 μm, were grown as described in Ref. [47]. A circular Teflon cell of diameter 14 mm (area 1.54 cm^2) was loaded with a 25-μl latex suspension with a particle volume fraction of 0.01.

The crystalline structure of the samples was studied by scanning electron microscopy (SEM 820, JEOL), transmission electron microscopy (TEM 1200 EX-II, JEOL) and AFM (Seiko). Vacuum evaporated carbon and gold films of a thickness of about 5 nm subsequently coated the latex arrays for SEM. For TEM, the crystal was first coated with carbon film and then removed from the mica plate together with the coating by floating the film on the water/air surface.

Results and discussion

Stages of crystal growth

After loading, the suspension spreads on the substrate over the entire cell area. Just after spreading the average thickness of the suspension layer is much larger than the latex particle size. Therefore, there is an induction period of water evaporation from the suspension before the start of crystallization. During this period, which lasts about several minutes depending on the humidity (Table 2), the suspension layer decreases in thickness, whereas the particle concentration increases; however, the layer remains thick enough everywhere allowing Brownian motion of the latex particles without constraint.

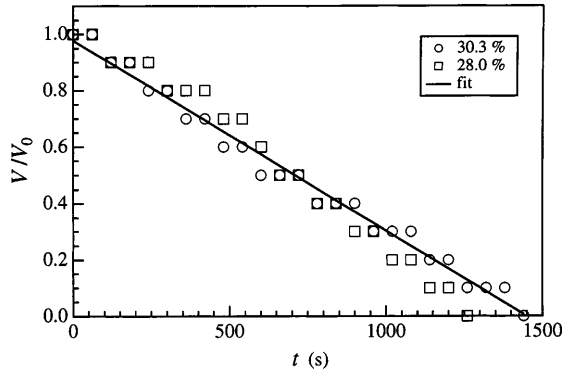

Fig. 2 Evaporation of water droplets of initial volume $V_0 = 1$ μl at various air humidities f_0. The stepwise appearance of data points is due to the limited accuracy in measuring the droplet weight. The *solid line* is a fit according to Eq. (2)

The scenario of the crystal growth process with submicron-sized particles is schematically summarized in Fig. 3 based on the results of this study and previous work [48, 49]. Crucial for the 2D crystallization is the final stage of thinning, when the suspension layer thickness becomes less than 1 μm in the cell center. Since the suspension layer near the cell periphery is thicker, the meniscus in the center starts to "feel" the substrate earlier. At a certain moment interference fringes (Newton rings) are observed to appear and expand at the spot of closest contact between the concave suspension/air interface and the substrate (Fig. 3a). Usually this spot is near the cell center but it can also be located closer to the cell periphery for an asymmetrical meniscus. The fringes of maximum or minimum intensity are loci of points for which the distance h_i between the two reflecting surfaces, meniscus and substrate, is $h_i = i\lambda/4n$. Here $n = n_p\varphi + n_w(1 - \varphi)$ is the refractive index of the latex suspension with n_p being the particle refractive index from Table 1 and $n_w = 1.3334$ – the index of refraction of water. The interference order, i, is odd for the dark fringes and even for the bright ones. Initially the fringes surround the meniscus apex (Fig. 3a), but several seconds later a plane-parallel film forms due to the interaction between the meniscus and the substrate. The initial film radius of

Table 2 Experimental parameters for 2D crystals of submicron latex particles. All crystals were produced from a suspension of initial volume fraction of latex $\varphi_0 = 0.001$ except crystals 6 ($\varphi_0 = 0.0005$) and 7 ($\varphi_0 = 0.01$)

d (nm)	Crystal no.	Substrate	f (%)	τ_e^a (min)	τ_c^b (min)
144	1	Glass	27	22	13
	2	Glass	35	20	17
	3	Glass	30–71[c]	30	23
	4	Glass	30–96[c]	40	40
	5	Mica	33	14	17
	6	Mica	41	27	17
	7	Mica	47	32	20
55	8	Glass	26	19	11
	9	Glass	60	50	18
	10	Glass	64	30	20

[a] Evaporation time elapsed from the loading of the crystallization cell with suspension until the appearance of interference fringes
[b] Crystallization time elapsed from the appearance of interference fringes until the cell area is completely covered by the crystal
[c] The first value corresponds to atmospheric humidity f_0 before closing the cell; the second value f is calculated at the end of crystallization using Eq. (1). The humidity is varied by closing the system with a petri dish of volume $V_a = 72$ cm^3 (sample 3) and $V_a = 47$ cm^3 (sample 4)

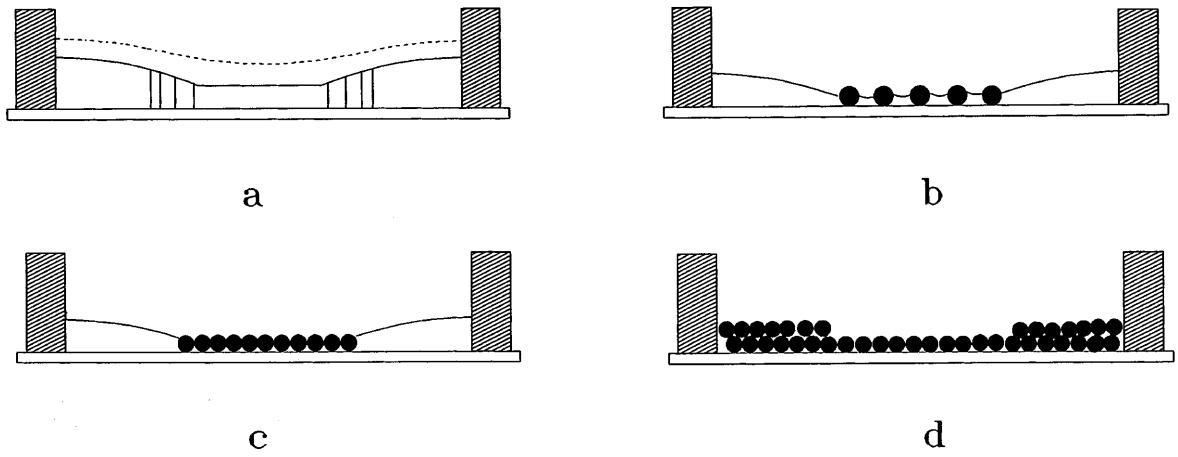

Fig. 3a–d Stages of the crystallization process illustrated with values of the film thickness h and time t typical for crystals of 144-nm particles grown at a humidity of about 30%. **a** Thinning of the suspension layer from its initial thickness $h_0 \sim 317$ μm ($t_0 = 0$). The first interference fringes appear at a distance between the meniscus apex and substrate $h_1 \sim 500$ nm ($t_1 - t_0 \sim 15$ min). Then a plane-parallel film of thickness $h_2 \sim 160$ nm forms ($t_2 - t_1 \sim 10$ s). **b** Association of the latex particles in the thin film due to a capillary force acting along the micromenisci. The nucleation is of duration $t_3 - t_2 \sim 5$ s. **c** Growth of a dense monolayer of hexagonal packing until appearance of the first bilayer at $t_4 - t_3 \sim 1$ min. **d** Growth of a multilayer latex crystal until the crystal border reaches the cell wall at $t_5 - t_4 \sim 15$ min

about 100 μm increases with time. The film thins within several seconds until latex particles in the film protrude from its surface, being constrained from below by the substrate. Using interference data for fringes and assuming circular symmetry, the meniscus profile can be computed by numerically solving the Laplace equation of capillarity [49]. The result of the calculations is that the film thickness remains equal to the particle diameter while micromenisci form around the particles (Fig. 3b). The menisci mediate an attraction between the particles originating in the capillary immersion force [46, 52–54]. This force collects the particles into an initially ordered monolayer (nucleus), Fig. 3c, which further promotes crystal growth. The particles are carried toward the crystal boundary by a water flow, which is to replace the water evaporated from the crystal surface. Entering the closest vicinity they are caught by the capillary force there and are attached to the crystal border to increase the monolayer area. Therefore, to grow a uniform monolayer one should keep the thickness of the suspension layer near the crystal border almost equal to the particle diameter. However, when the border approaches the cell wall, the meniscus slope increases thus resulting in the simultaneous formation of two particle layers (bilayer), followed by a triple layer, etc. (Fig. 3d).

The crystallization of 144-nm (Fig. 4) and 55-nm latex particles (Fig. 5) follows the scenario from Fig. 3. The thin liquid film is of circular or elliptical shape depending on the meniscus profile. Figures 4a and 5a show such films just before the start of nucleation. The film with 55-nm particles is dark because its thickness is less than that corresponding to the first interference minimum. Figures 4b and 5b illustrate monolayer nuclei, which also contain voids (bare substrate). This can be explained by a deficiency of particles at the spot of nucleation [49]. Initially there is no convection since the ordered array is of too small a mass to initiate the influx of water, and thus of particles, toward the crystal. In contrast, for a prevailing convective supply of particles a dense monolayer grows. When the crystal border approaches the cell periphery, a particle multilayer starts to form (Figs. 4c, 5c) due to growth instability as described later. The final crystal consists of a monolayer in the center surrounded by ring-shaped multilayers (Figs. 4d, 5d).

Similar trends have also been observed in the growth of monocrystals of micron-sized latex with a few differences arising from the particle and cell diameter (14 mm). Initially, there is an increase in the local particle density at the point of closest approach between the meniscus and the substrate (Fig. 6a). Since the particles are too big to maintain a plane-parallel film, nucleation is a much slower process, taking place over a rather large area (Fig. 6b). The lateral capillary force governs the formation of islands of ordered particles as well as their subsequent merging into larger structures, including voids (Fig. 6c). Once the central monolayer becomes denser, convection-dominated growth starts, which leads to the final monocrystal represented in Fig. 6d. Decreasing the cell diameter to 2 mm, but maintaining the other conditions, makes the crystal growth irregular (Fig. 7).

Effect of solvent evaporation

The crystal structure and quality are mainly affected by the rate of crystallization, which is determined in turn by

the evaporation rate. By changing the humidity the total time of crystallization can vary over a fairly wide range: from several minutes to several hours. Nevertheless, structured domains can always be found using an electron microscope, at least locally; however, the best structure of the grown crystal is achieved at a high crystallization rate (air humidity of about 30% or less).

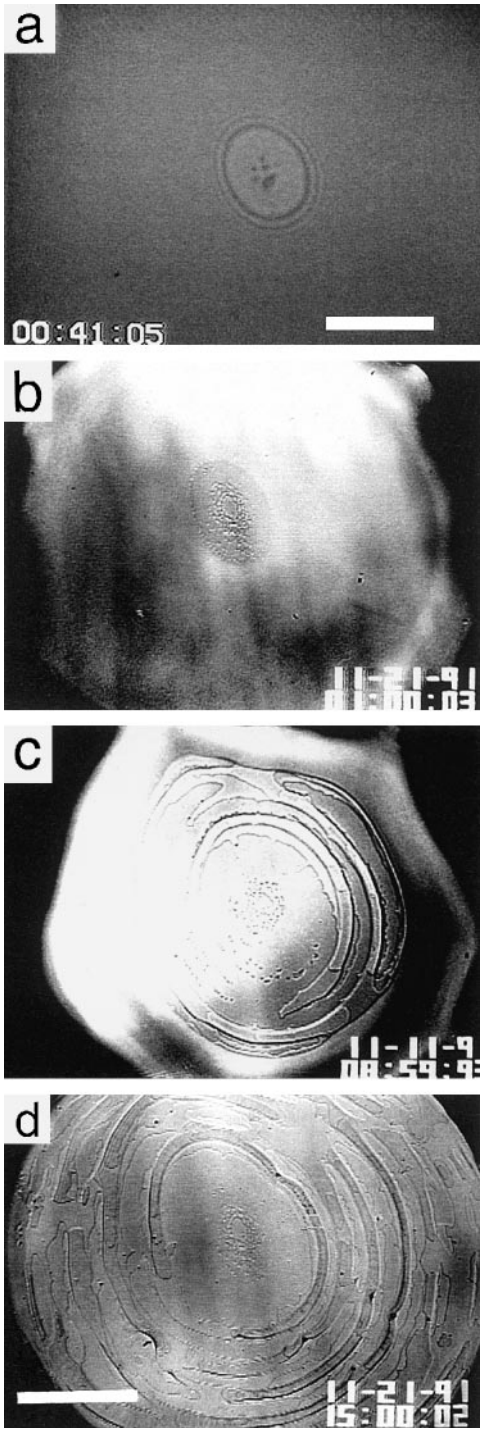

These crystals look colored when observed by the optical microscope in reflected light. Each color corresponds to a film of fixed crystalline lattice and number of particle layers [62]. An SEM study of the samples of 144-nm particles shows that a crystal layer has a uniform structure on a large scale with a typical size of about 100 μm. The defects in the crystal lattice, considered later, disturb only the local order. When the rate of crystallization decreases, the crystal structure becomes worse. For example, the crystals, grown for more than 1 h, are only of local order (a few microns). Such crystals are disordered on a large scale; this is also supported by optical observation (cf. Fig. 8). The macroscopic defects (cracks, whiskers, layers of irregular shape, etc.) make the crystals colorless by disturbing their structure.

The humidity regulates the rate of water evaporation and thus the convective influx of particles. Experimental results for the crystal radius $R = \sqrt{A/\pi}$ at different humidity are shown in Fig. 9 for 144-nm particles. The crystal grown at the lowest humidity exhibits the highest crystallization rate, which can be explained by the largest influx of particles. Respectively, the rate of crystallization is slowed down at suppressed evaporation (high humidity). The same conclusion can also be drawn from the kinetics curves in Fig. 10 for crystals of 55-nm particles produced at different humidities.

The crystallization rate K was calculated from the experimental data using the equation

$$R(t) = R_0 + Kt \ , \tag{3}$$

which shows R increases linearly with time t. On the other hand, a simple theory [48] relates K to microscopic parameters of the crystal and the hydrodynamic flow

$$K = \frac{w_w j_e \beta l \varphi}{h(1-\varepsilon)(1-\varphi)} \ . \tag{4}$$

Here $\beta = v_p/v_w$ is the ratio between the hydrodynamic velocity of particles, v_p, and that of water flow, v_w, ($\beta \leq 1$). Particles of smaller hydrodynamic resistance should exhibit larger β, i.e. $v_p \sim v_w$. φ is the particle volume fraction in the suspension. h is the average

◄

Fig. 4a–d Successive photographs of the growth of a 2D crystal of 144-nm latex particles. **a** Thin liquid film of thickness $h \sim 160$ nm just before the start of nucleation ($t = 7$ s). The photograph is taken in reflected monochromatic light at the moment of appearance of the first interference fringes (sample 5 from Table 2, *bar* 0.2 mm). **b** 2D nucleus at $t = 1$ min. The *spots* inside the nucleus are voids (bare substrate) surrounded by a dense particle monolayer. The *space* outside the nucleus is occupied by the latex suspension. **c** Growth of an abundant crystal at $t = 8$ min. The monolayer nucleus from **b** remains in the crystal *center*. Multilayer rings are observed to form. **d** Final crystal at time $t = 15$ min representing a sequence of six multilayer rings surrounding the central monolayer. Photographs **b**–**d** were taken in transmitted light (sample 2; *bar* 0.25 mm)

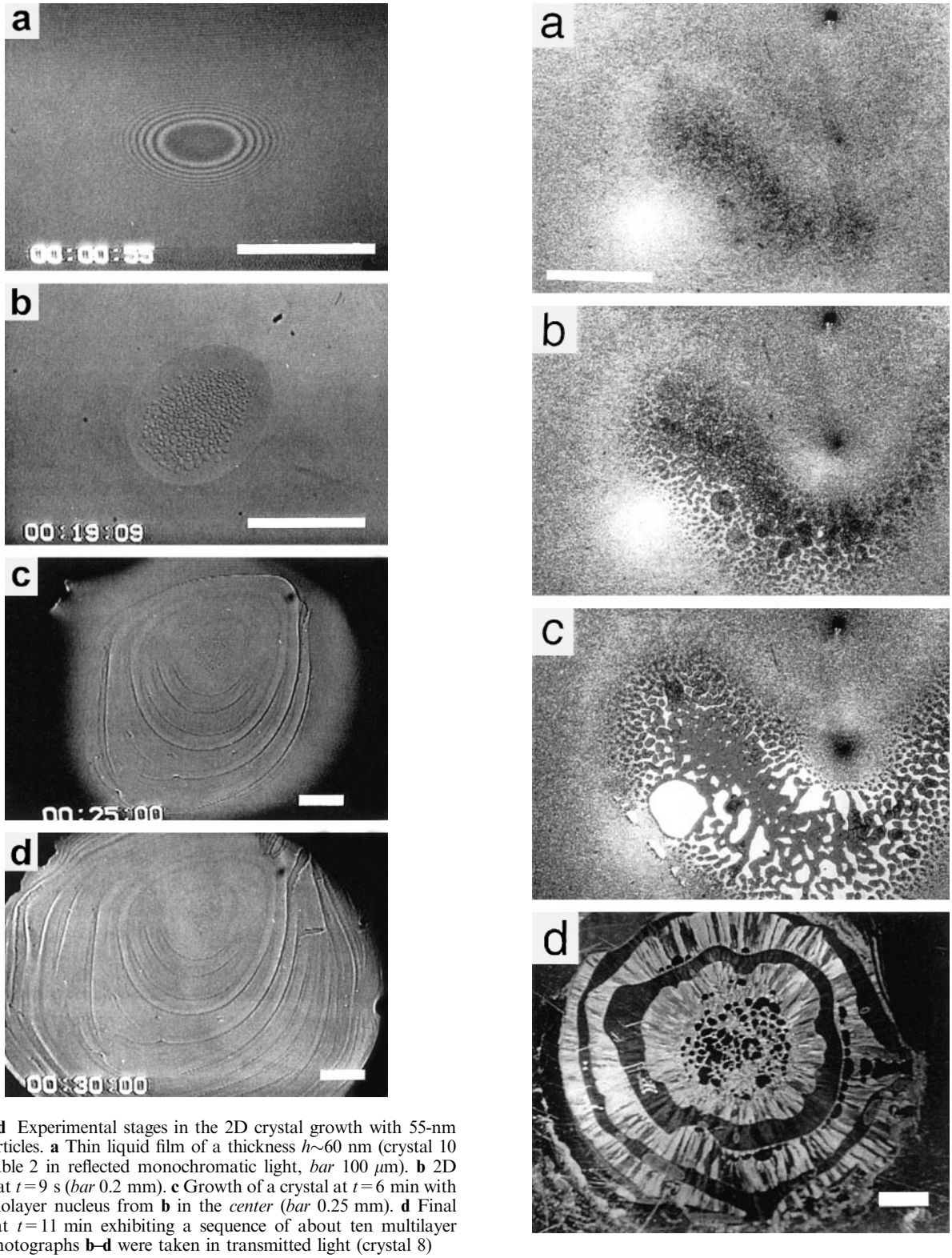

Fig. 5a–d Experimental stages in the 2D crystal growth with 55-nm latex particles. **a** Thin liquid film of a thickness $h \sim 60$ nm (crystal 10 from Table 2 in reflected monochromatic light, *bar* 100 μm). **b** 2D nucleus at $t = 9$ s (*bar* 0.2 mm). **c** Growth of a crystal at $t = 6$ min with the monolayer nucleus from **b** in the *center* (*bar* 0.25 mm). **d** Final crystal at $t = 11$ min exhibiting a sequence of about ten multilayer rings. Photographs **b–d** were taken in transmitted light (crystal 8)

crystal thickness. ε is the average crystal porosity defined as the ratio between the volume of pores (voids) and the total crystal volume. l is the width of a ring domain of area $A_e \approx 2\pi Rl$, located at the crystal periphery, which effectively participates in the evaporation of water. The rest of the crystal located at $r < R - l$ is considered as

◀

Fig. 6a–d Growth of a crystal of 1.696-μm latex particles on mica from a suspension of initial volume $V_0 = 25$ μl and volume fraction $\varphi_0 = 0.01$ spread in a cell of diameter 14 mm. **a** Start of the nucleation ($t_0 = 0$). **b** Growth of particle islands ($t = 1$ min). **c** Growth of a monolayer ($t = 1.5$ min). Photographs **a–c** were taken in transmitted white light (*bar* 0.3 mm). **d** Final dry crystal in transmitted white light (*bar* 2 mm). The illumination at a certain angle reveals the crystalline domains of different diffraction colors

almost dry. The dependence of K on humidity comes from $j_e(t) = j_{e0} \exp(-t/\tau_e)$.

Based on Eq. (4) one can understand the experimental facts listed in Tables 2 and 3. At the same low humidity, the rate of crystallization, observed with 55-nm particles seems larger than the respective rate with 144-nm particles. Assuming the other parameters are the same, the 55-nm particles have larger β due to their smaller hydrodynamic resistance and, hence, K is also larger. At high humidity there is a difference between the kinetics curves in Figs. 9 and 10. Samples 3 and 4 are produced in a closed system of humidity increasing with time (Table 2), whereas samples 9 and 10 are grown in an open system of high constant humidity. There is very

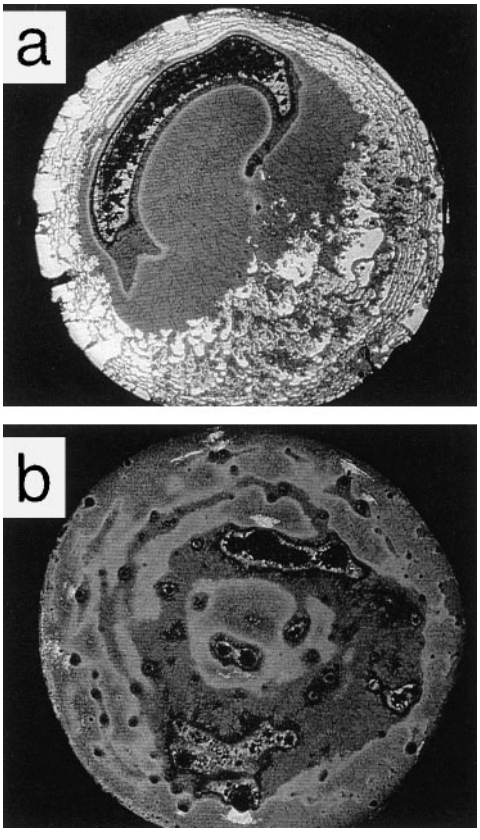

Fig. 7 Latex crystals of 1.696-μm particles grown on glass in a cell of diameter 2 mm from a suspension of volume $V_0 = 1$ μl and different initial volume fraction: **a** $\varphi_0 = 0.005$; **b** $\varphi_0 = 0.01$

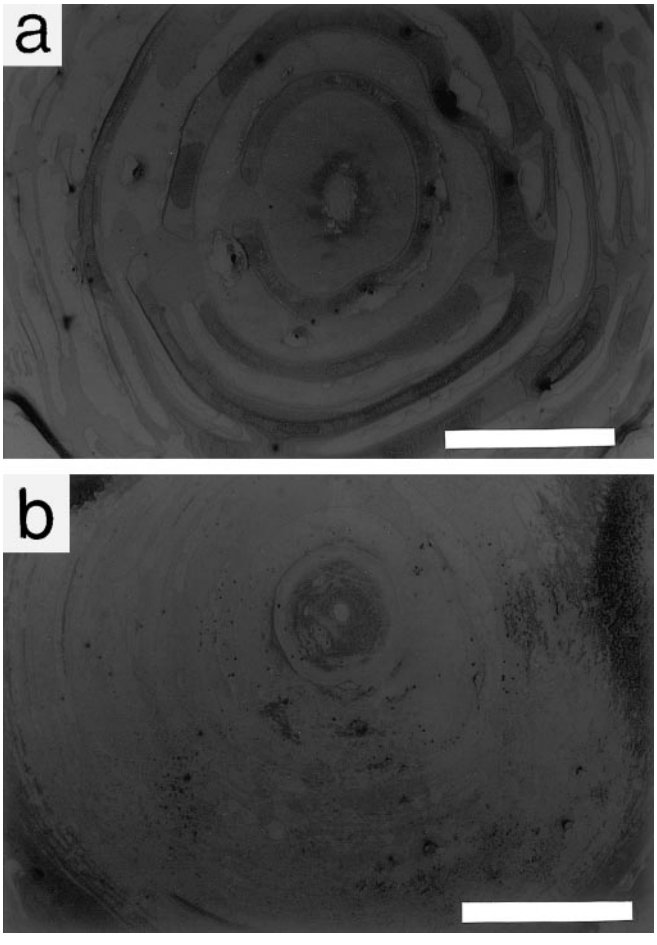

Fig. 8 Comparison of two latex crystals of 144-nm particles grown on glass at different humidities: **a** 30%; **b** 71%. A difference in the crystallinity, which is better in **a**, leads to the different interference colors observed in white reflected light

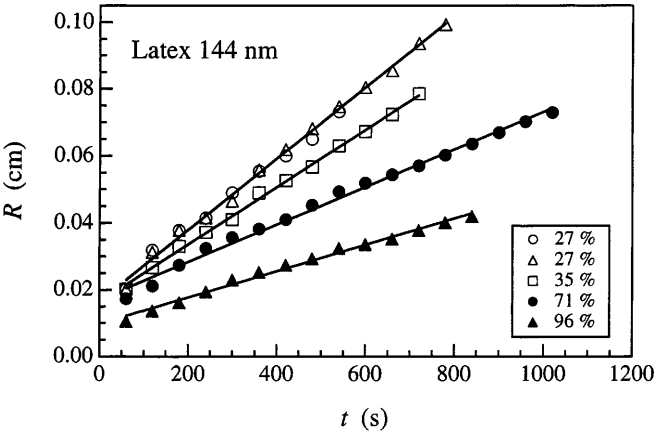

Fig. 9 Time-dependence of the radius of 144-nm latex crystals grown on glass at different humidities. The area of crystal 1 ($f = 27\%$) is measured both by an image analyzer (*open circles*) and by a caliper gauge (*open triangles* [48])

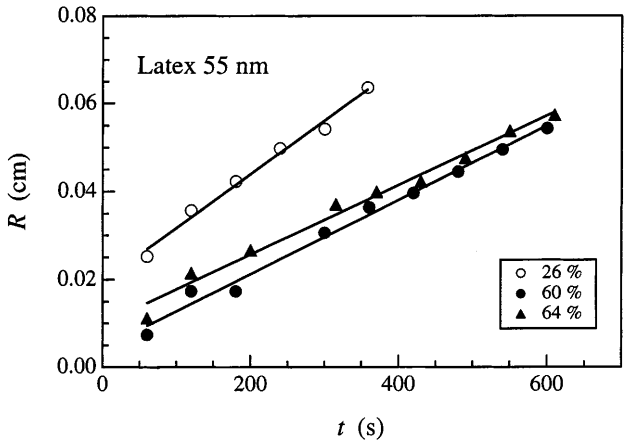

Fig. 10 The radius of 55-nm latex crystals grown on glass at different atmospheric humidities

Table 3 Calculated parameters for 2D crystals of submicron latex particles

d (nm)	Crystal no.	R_0 (cm)	K (cm/s)	τ_c^a (min)	τ_c^b (s)
144	1	1.66×10^{-2}	1.07×10^{-4}	13.0	13
	2	1.63×10^{-2}	0.86×10^{-4}	16.2	17
	3	1.71×10^{-2}	0.56×10^{-4}	24.7	23
	4	0.97×10^{-2}	0.40×10^{-4}	37.6	40
55	8	1.95×10^{-2}	1.22×10^{-4}	11.0	11
	9	0.43×10^{-2}	0.84×10^{-4}	19.0	18
	10	0.99×10^{-2}	0.79×10^{-4}	19.0	20

[a] Crystallization time calculated using the equation $\tau_c = (R_c - R_0)/K$, cf. Eq. (3), with a cell radius $R_c = 0.1$ cm and values of R_0 and K from the table
[b] Total crystallization time measured experimentally (see Table 2)

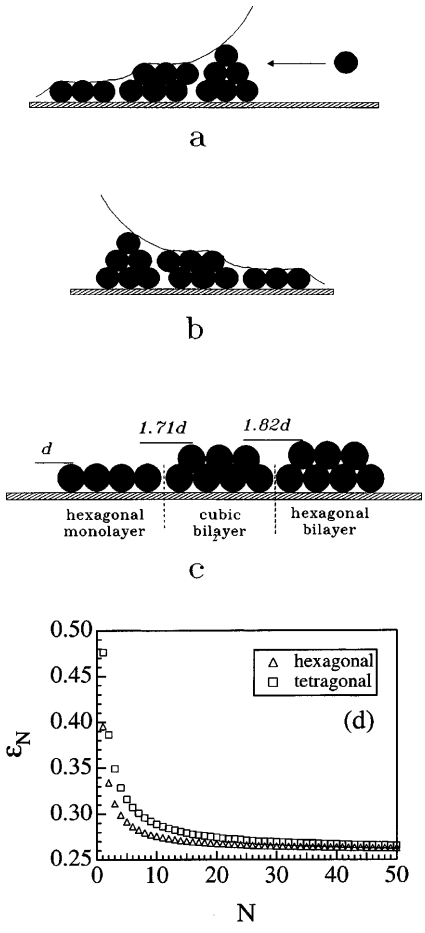

Fig. 11a–d Formation and structure of a multilayer ring. **a** Increase in the number of particle layers (advancing meniscus). **b** Decrease in the number of layers (receding meniscus). **c** Transition zone between a monolayer and a bilayer. **d** Dependence of the crystal porosity on the number of latex particle layers illustrating a smooth transition from a 2D to a 3D crystal structure

good agreement between the total crystallization time, τ_c, measured experimentally (Table 3), and the one calculated based on the local crystallization rate, K, that is more difficult for a direct measurement.

The initial nucleus radius, R_0, listed in Table 3 seems to be of the same order as the radius of the thin liquid film preceding the nucleation (cf. Figs. 4a, 5a). At high humidity this radius is smaller than at low humidity suggesting the lack of a plane-parallel film and, hence, of good nucleation.

If the atmospheric humidity is too high, the use of a dry gas accelerates the growth process. With gas of $f \approx 0$ the rate of crystallization increases 3–4 times compared to the reference $f = 30\%$. With dry nitrogen, however, a lot of gas bubbles of diameter of about 1 μm are observed to form in the suspension. These bubbles rupture when crossing the crystal border thus causing circular disturbances in the crystal lattice observed by SEM. To avoid gas bubble formation oxygen is used. In the presence of dry oxygen crystals with very good colors have been grown with 55-nm particles on different substrates: bare glass and mica, glass coated with thin carbon or gold layers [62].

Effect of the meniscus shape: growth instability

Although the crystal growth is determined by the evaporation rate, the meniscus slope near the crystal boundary affects the number of particle layers (Fig. 3). Approaching the cell periphery, the meniscus slope increases, which favors a multilayer formation (Fig. 11a). It takes more and more particles to maintain the growth of a structure with a gradually increasing number of layers. Since the convective water flux remains nearly constant, it cannot supply particles in a concentration high enough to feed the growing multilayer. There is a threshold beyond which the process is

reversed, leading to a fast decrease in the number of crystal layers (Fig. 11b). The meniscus slope changes so rapidly that it could even become detached from the crystal boundary, leaving empty sites behind the multilayer ring (Fig. 8a). Soon after a new monolayer forms followed by subsequent rings repeating the scenario described above. As a result, the multilayer rings have outer slopes much steeper than the inner ones. Depending on the conditions, different numbers of rings, M, can be observed (Table 4): up to 5–6 multilayer rings in crystals of 144-nm particles (Figs. 4d, 8a) and up to 9–10 rings in crystals of 55-nm particles (Fig. 5d). A multilayer ring comprises various numbers of particle layers, N: no more than 4–5 layers of 144-nm latex particles or more than ten layers of 55-nm particles (Table 4). Similar multilayers can also be found in the crystals of micron-sized particles (Fig. 6d). In this case there are no more than two pronounced rings of (mainly) bilayers although the crystal area is much larger. Hence, the number and width of multilayer rings depend on the particle diameter, d, and the crystallization cell radius, R_c. Decreasing the particle size increases the number of successive rings, as well as the number of layers in one ring.

Figure 12a represents the local rate of crystallization, $K = dR/dt$, measured along a radial line drawn across the multilayer rings in Figs. 4d and 5d. Here $R(t)$ is taken as the distance between the nucleus center and the front of crystallization. The formation of a multilayer can be identified from the decreased rate of crystallization. The layers of 55-nm particles are formed at larger local rates, in accordance with the previous section. Although the local rate of crystallization is sensitive to the layer number, the total crystal area, $A(t)$, seems not to be affected. It is an average result from the growth rate in all crystal directions which are of nonuniform layer distribution.

The radial periodicity in the number of crystal layers, observed by us, is evidence for a sort of growth instability. The hydrodynamic instability observed in an oil layer of millimeter thickness placed in a circular cell with a temperature gradient across the layer [63] has a similar pattern. In that case the instability waves are concentric circles visualized by fine particles suspended in the oil. To prove whether the instability observed by us can also be due to a temperature gradient introduced by the illuminating light, we performed independent experiments in complete darkness. Since the same multilayer rings were obtained, one can conclude that the mass transfer should drive the crystal growth instability. The competition between the particle transfer and contact line motion finely regulates the meniscus profile up and down, creating the multilayer rings; this is why the smaller particles are more sensitive to variations in the meniscus profile. On the other hand, the cell size also seems to be of importance for the instability ring number.

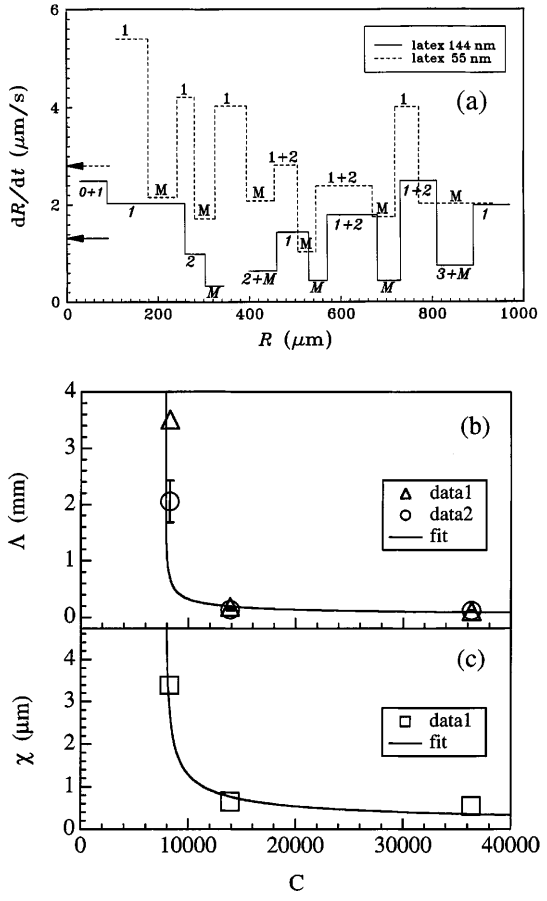

Fig. 12a–c Crystal growth instability. **a** The linear rate of crystallization, measured radially for the crystals in Figs. 4 and 5 as a function of the distance from the nucleus center. The *arrows* indicate the mean linear rate of crystallization. *1* – monolayer; *2* – bilayer; *3* – triple layer; *M* – multilayer. *Italic letters* are for 144-nm particles, *normal letters* are for 55-nm particles, respectively. **b** The characteristic instability length as a function of the ratio of the cell and particle diameters. Data set 1 is the average length estimated from the data in Table 4. Data set 2 is measured from **a** and Fig. 6d with the *error bars* representing the standard deviation. The *solid line* is a fit using Eq. (5) with parameters $C_0 = 7800$ and $\Lambda_0 = 15$ mm. **c** The average height of a multilayer ring versus the same dimensionless ratio. The *solid line* is a fit according to Eq. (6) at $\chi_0 = 60$ μm

Table 4 Parameters of cells and multilayer rings formed under various conditions

R_c (mm)	A_c (mm^2)	V_0 (μl)	h_0^a (mm)	d (nm)	M	N
1	3.14	1	0.317	55	9–10	>10
				144	5–6	4–5
				1696		
7	153.9	25	0.162	1696	2	2

[a] Average initial thickness of the suspension film calculated from $h_0 = V_0/A_c$

Any instability can be quantitatively described by defining its characteristic length $\Lambda = R_c/M$. Unlike in another case [63], the 3D instability patterns, multilayer particle rings, reported by us can also be characterized by their height $\chi = dN$. Both Λ and χ are averaged quantities. For example, Λ estimated from this definition (data 1 in Fig. 12b) can differ from its value measured from the local crystallization rate in Fig. 12a (data 2 in Fig. 12b), especially for micron-sized particles. Also, the definition of χ should be considered as an upper estimate of the ring height, which depends on the type of packing in the crystalline lattice [62]. Nevertheless, the plot of Λ and χ versus the dimensionless number $C = 2R_c/d$ in Fig. 12b, c, respectively, represents the main features of instability. There is a minimum number $C_0 = 7800$, below which Λ tends to infinity, i.e. no rings can be observed because the instability length becomes larger than the cell radius R_c. For this reason, there are no periodic rings of micron-sized particles in a cell of diameter $2R_c = 2\,\text{mm}$ (Fig. 8a), where $C = 1179$ is much smaller than C_0. Also, with increasing C, for example, by decreasing d or increasing R_c, Λ goes to zero, which makes the circular rings indistinguishable. This is the case of submicron-sized particles, $d = 144$ nm, in a cell of diameter $2R_c = 14\,\text{mm}$, where $C = 97222$.

This behaviour of Λ and χ is satisfactorily described by the empirical equations

$$\Lambda = \Lambda_0/\sqrt{C - C_0} \tag{5}$$

$$\chi = \chi_0/\sqrt{C - C_0}\ , \tag{6}$$

where Λ_0 and χ_0 are characteristic scales. Both quantities, $\Lambda(C)$ and $\chi(C)$ have the same functional dependence on the dimensionless number C. To understand the origin and also the meaning of the parameters C_0, Λ_0 and χ_0, one needs to consider deeper the hydrodynamics of flow in the suspension surrounding the growth of the monocrystal. An attempt in a similar direction is the quantitative model [64, 65] describing the growth of multilayer strips on the periphery of a shrinking suspension droplet freely spread on a solid substrate – a case opposite to our geometry; however, that model considers a unidirectional horizontal flow of particles, which explains only the length, Λ, of strips (rings). To account for the variations in the film thickness, $h(t)$, which determines the ring height, χ, one should also consider a vertical flow in a curved liquid film.

The instability can be avoided and well-ordered monolayers can be grown if one keeps a uniform meniscus profile in the cell, for example, by gently sucking or adding liquid [28]. One elegant method for building up a large-scale monolayer is by continuously assembling the particles at a meniscus shape precisely controlled corresponding to the growth rate. This has been done, for example, on a solid substrate dipped [56] or rotated [58, 59] in the suspension.

Effect of particle concentration and substrate

The crystals grown on mica from 144-nm particle suspensions of different concentrations are compared in Figs. 13 and 14. Although the crystal radius as a

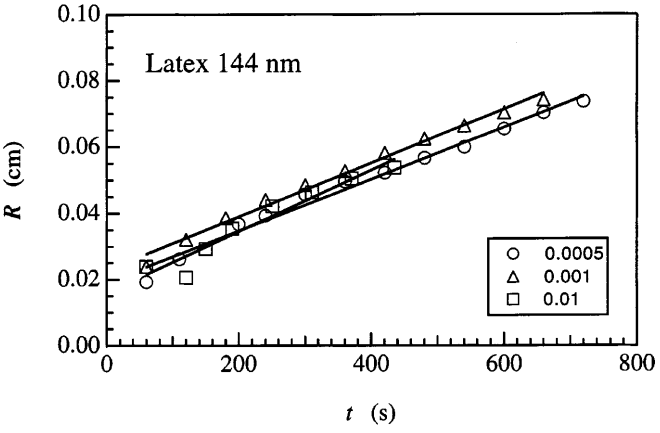

Fig. 13 The radius versus time for crystals grown on mica at different volume fractions of 144-nm latex particles (the growth parameters are shown in Table 2)

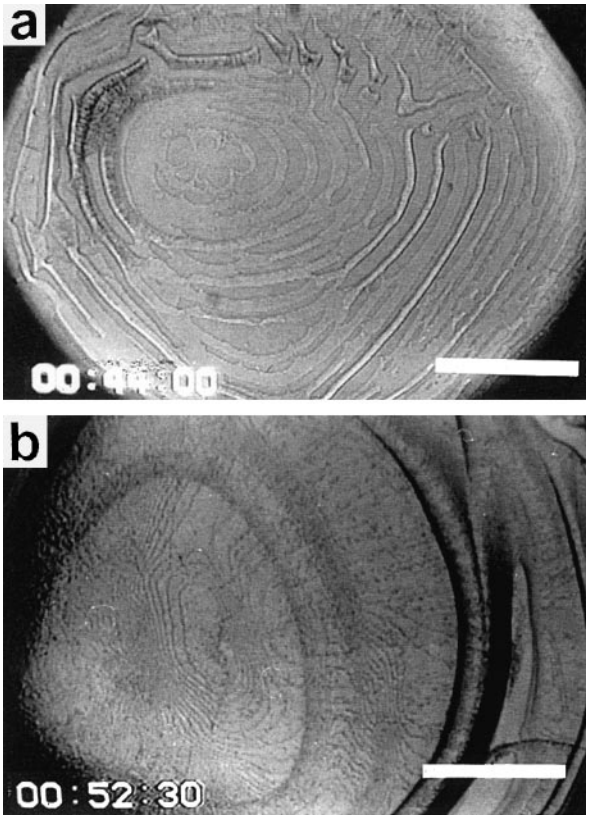

Fig. 14a, b Latex crystals of 144-nm particles grown on mica from suspensions of different volume fractions **a** $\varphi_0 = 0.0005$ (sample 6), **b** $\varphi_0 = 0.01$ (sample 7). *Bars* 0.25 mm

function of time is not so sensitive to a variation in the particle concentration, the optical observations show a difference in the crystal structure. An initial volume fraction of latex of $\varphi_0 = 0.0005$ is not enough to produce a dense crystal. In this case the growth instability manifests itself as strips of ordered particles (mainly monolayer) separated by a bare substrate (Fig. 14a). At a very large particle fraction, $\varphi_0 = 0.01$, a thick multilayer of latex remains on the substrate after drying (Fig. 14b). Increasing φ_0 suppresses the growth instability or makes it less pronounced (cf. Fig. 7b for micron-sized latex). $\varphi_0 = 0.001$ seems the most appropriate fraction for producing crystals of good quality in the 2-mm crystallization cell (Fig. 4). This concentration effectively corresponds to a coverage of 3.4 particle layers, if the area per particle is 1.8×10^{-10} cm^2 and the total number of particles in 1 μl suspension is 6.0×10^8.

The same particle concentration ($\varphi_0 = 0.001$) turns out to be also appropriate for a good crystal of the 55-nm latex. In this case the area is covered by 18.2 particle layers on average (area per particle 5.2×10^{-11} cm^2, total number of particles in 1 μl suspension 1.1×10^{10}). What seems important is the total volume of latex particles, if the solid material follows the shape of the meniscus during drying.

The substrate (glass or mica) introduces a slight difference into the crystallization process. The crystals on mica often contain voids. With submicron-sized particles such defects form when the meniscus is detached from the first multilayer, after which the contact line moves freely on the mica surface with no particle layer remaining. It can be seen with micron-sized latexes that the moving line pushes aside the particles. The reason for not-so-tight sticking to the substrate is the electrostatic repulsion between the particles and the mica surface, which also bears negative charge.

Crystalline structure and defects

The crystal layers have predominantly hexagonal lattices as confirmed by the microscopic observations (Fig. 15). Normally, a crystal of 144-nm latex particles has better ordering than a one of 55-nm particles grown under the same conditions. One reason is that the 55-nm latex is less monodisperse, and this cannot be improved by filtration. Another reason is the presence of a stabilizing agent, which the 55-nm latex suspension should contain. This agent most probably restricts the free motion of particles and clusters, thus disturbing their close packing. The agent present on the mica surface after drying explains the poorer contrast of the TEM micrograph as well. A third reason is the shrinkage of latex particles at complete drying, or heating by an electron beam [35], which is more pronounced with a smaller latex. Last, but not least, the smaller the particles the stronger the

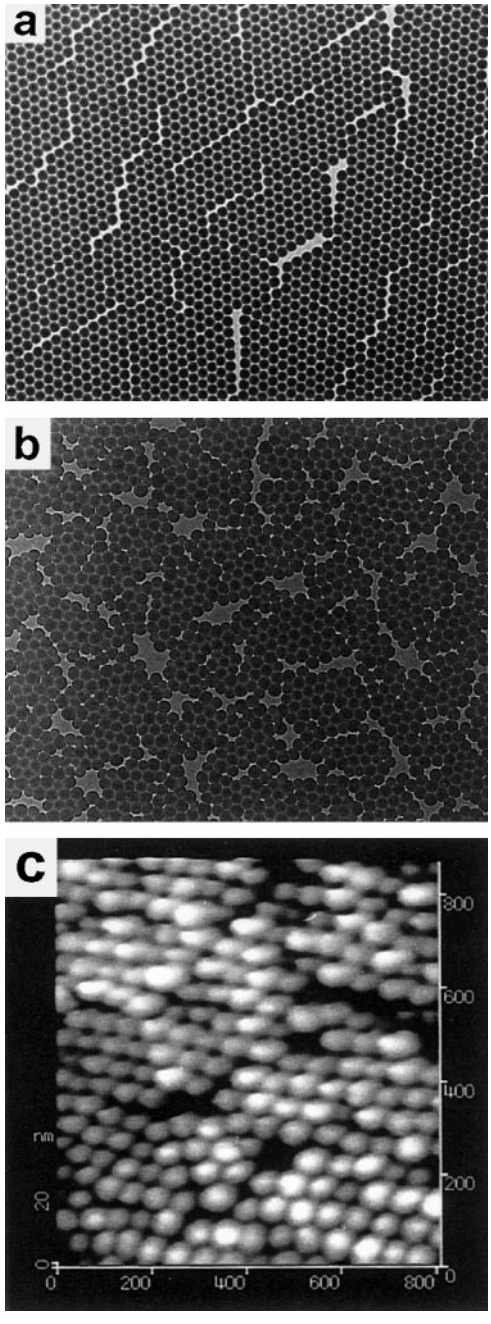

Fig. 15a–c Structure of latex monolayers Transmission electron microscope (*TEM*) micrographs of **a** 144-nm and **b** 55-nm latex particles originally deposited on mica. **c** Atomic force microscope micrograph of 55-nm particles on glass

Brownian motion opposing the convective flux and promoting structural defects.

In the transition zone between two multilayers one can always observe a square (tetragonal) lattice (Fig. 16). SEM and TEM observations confirm that the number of square-packed layers in a dry crystal obeys the sequence described for wet layers between

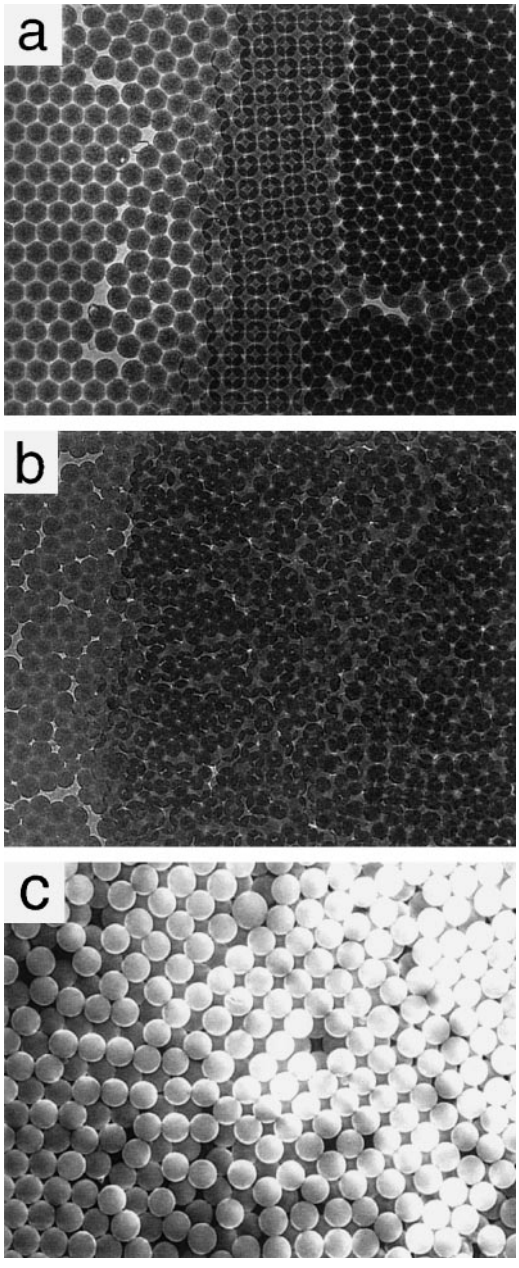

Fig. 16a–c Square lattice located in the transition zone between a monolayer (*left*) and a bilayer (*right*): TEM micrographs of **a** 144-nm and **b** 55-nm latex particles originally deposited on mica. **c** Scanning electron microscope (*SEM*) micrograph of 1.696-μm latex particles on glass

concave or inclined solid surfaces [20–22]. Hence, the layers of square packing acquire an intermediate thickness compensating the liquid meniscus slope, which plays the same role of an upper boundary surface in our experiment (Fig. 11c). From a thermodynamic point of view, the square lattice does not seem stable to predominate over a large area, unless it is constrained between two successive layers of hexagonal packing.

These observations suggest a local porosity, ε_N, depending on the number of particle layers, N, and their crystalline structure. For a monolayer of hexagonal packing $\varepsilon_1 = 1 - \pi/3\sqrt{3} = 0.3954$, whereas for square packing $\varepsilon_1 = 1 - \pi/6 = 0.4764$. For the respective multilayers ε_N can be calculated using the equations

$$\varepsilon_N = 1 - \frac{\pi N}{3\left[\sqrt{3} + (N-1)\sqrt{2}\right]} \tag{7}$$

for hexagonal close packing and

$$\varepsilon_N = 1 - \frac{\pi N}{3\left[2 + (N-1)\sqrt{2}\right]} \tag{8}$$

for tetragonal close packing [62]. Increasing the layer number N decreases ε_N while increasing the crystal density (Fig. 11d). In the limit of a bulk crystal, $N \to \infty$, both Eqs. (7) and (8) tend to the same value: $\varepsilon_\infty = 1 - \pi/3\sqrt{2} = 0.2595$. To reach this limit with an accuracy of 1% one needs 60 layers at least, much more than the average number of layers composing our 2D crystals.

It is a well-known fact that real crystals always have defects. For example, some metal crystals contain up to 10^{12} dislocations per square centimeter [1]. Similarly, the 2D crystals of latex particles also exhibit different defects, which are poorly described in the literature, usually emphasizing a perfect structure rather than deviations. Knowing the nature of the defects, however, one can try to reduce them by avoiding the conditions for their formation. Except for the empty sites (bare substrate), described in the previous sections, we observe several other defects in the latex crystals:

1. Point defects. If a particle is missing from the crystal lattice (Fig. 17a), a vacancy is formed as in the case of an atomic crystal [1]. More vacancies are observed with micron-sized latex particles than with submicron-sized ones, probably because the friction between a particle and the substrate is larger in the first case than in the latter [66]. Another defect, called by us ''replace'', arises when a latex particle is replaced by a particle of different size: larger or smaller (Fig. 17b). The replace is due to the latex polydispersity and is analogous to the defect created by a doping atom [1].

The point defects could, in principle, be used for recording information. For example, a vacancy could be assigned as ''zero'' while the presence of a particle on the same spot could be ''unity''. Using a replace of smaller or bigger size than the standard one, the ''digits'' could be extended up to 4. To artificially create point defects and read the stored information one can manipulate the particles in an array using AFM.

2. Dislocations. There are two dislocation types. The first one we call primary dislocation, because it forms during the crystal layer growth, is also seen on the video. Primary dislocations separate big crystal do-

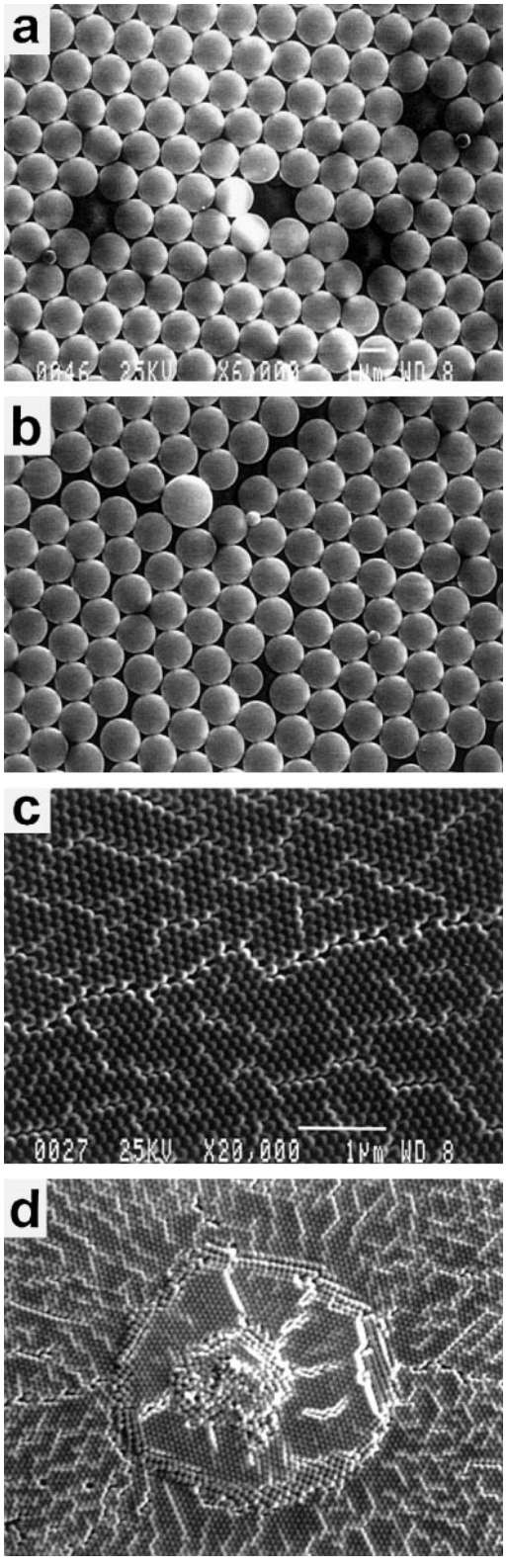

Fig. 17a–d SEM photographs of defects in 2D latex crystals. **a** Vacancies and **b** inserts, illustrated with particles of diameter 1.696 μm on glass. Primary dislocation **c** in a crystal monolayer and **d** a multilayer hill obtained with particles of diameter 144 nm on glass

mains of thousands of particles in a crystal of 144-nm or 1.696-μm particles (Fig. 17c). Such dislocations are observed in the monolayer, bilayer, triple layer, etc. A dislocation starts from the central nucleus and goes radially into the monolayer. Similarly, in the bilayer the dislocations start at the boundary with the monolayer. The total length of a primary dislocation can be about 10–100 μm. One possible explanation for the existence of dislocations is the restricted area of crystallization: the formation of a domain is influenced by the neighboring domains which form simultaneously on the substrate. On a local scale a particle can easily find its right position in the crystal lattice; however, it is impossible to precisely couple the rows and domains of many particles, which serve as the origin of dislocations along the line of coupling. Our experimental simulations of ordered domains and dislocations with much bigger particles support this point: glass balls of diameter of 3 mm. The monolayer "crystal" is formed by manipulating the particles on the bottom plane of a plastic box (about 30×50 cm). A dislocation appears at a dense coverage of the bottom area fully occupied up to the box walls. By shaking the box one can change the position and shape of the dislocations but cannot avoid them completely.

The second type, called secondary dislocation, looks like lines inside one crystal domain (cf. Fig. 15), and is much shorter than a primary dislocation. One possible reason for the secondary dislocations can be the alignment of subdomains in a crystal domain, as observed by optical microscopy during the growth of a crystal of micron-sized particles. Another reason can be the particle shrinkage in the course of latex drying.

3. Hills. They are macroscopic 3D defects in the crystal, looking like dark spots on the optical photograph, which are caused by particle aggregates. The latex particles coagulate in the suspension, if their local concentration strongly increases due to water evaporation. Such an aggregate resembles a hill of particles incorporated in the crystal (Fig. 17d). The meniscus around the aggregate is steeper than the meniscus in the vicinity of the monolayer thus initiating a multilayer. Enormous aggregates can disturb the crystal layers over a large area due to higher consumption of particles.

4. Various types of crystal lattice. Except at the boundary between two layers of hexagonal packing, one can observe domains of square lattices also inside a hexagonally packed multilayer. The crystal containing such inclusions is produced at a very low crystallization rate, suppressing the particle motion and domain alignment. A similar situation can be visualized with micron-sized particles in a suspension film containing glucose. The glucose strongly increases the suspension viscosity thus decreasing the velocity of particle motion. The motionless particles form domains of square packing which slowly disappear on realignment of the

crystal layer. Besides, some of the square domains remain "frozen" in the monolayer by the glucose.

SPR microscopy of monolayers of nanometer particles

A monolayer of nanometer-sized particles, for example, latex of size smaller than 55 nm, is invisible using an optical microscope, especially if it is deposited on a transparent substrate. A monolayer of 19-nm particles is hardly seen even if it is deposited on a reflective metal substrate – thin silver film (Fig. 18a). Details of the particle layer can be clearly seen, if one illuminates the silver film from below (opposite the particle layer side) by monochromatic light at an incident angle θ (Fig. 18b). At a certain angle bigger than the angle for total internal reflection (41.3°) a deep minimum of reflected light appears (Fig. 18c). The reason for this minimum, named SPR, is the generation of electron excitation (surface plasmon) in the metal film close to the boundary with the nanoparticle layer [67]. Using the Fresnel equations one can calculate from the reflectance data the particle layer thickness d and the complex refractive index $\hat{n} = n + ik$ [61] (i – imaginary unit). To do this, one should know in advance the corresponding parameters of the silver coating, which are determined from independent measurements of bare metal film.

The layer of 19-nm particles is deposited on a silver film with parameters $d_{Ag} = 55\,\text{nm}$, $n_{Ag} = 0.141$ and $k_{Ag} = 3.857$ – see the reference curve in Fig. 18c. The same parameters are also obtained from the reflectance, $\eta(\theta)$, measured at the center of the latex film: this is evidence for the lack of particles there. Two different points of the latex monolayer, located at the sample periphery, are then examined. The fits to the experimental data are drawn assuming a constant monolayer thickness equal to the particle diameter and adjustable optical constants. Close values of n and k have been calculated for both points (on average $n = 1.17$ and $k = 0.07$) implying uniformity of the latex monolayer. The value of n is smaller than the one predicted for a layer of closely packed polystyrene particles: $n = 1.4$ [62]. This means that the nanoparticle layer obtained by using surfactant is of lower particle density, i.e. higher porosity, due to the great number of voids seen in Fig. 18. Probably, the energy lost by light scattering from nonuniformities in the film determines the imaginary part k.

Details of the nanoparticle layer can be clearly seen by observation with SPR microscopy. The position of the minimum reflectance depends strongly on the thickness and the refractive index of the layer, for example, different structure. When one is close to this minimum, the latex film looks bright due to the maximum light scattered from it in a direction opposite the substrate. In this way, looking from above with an

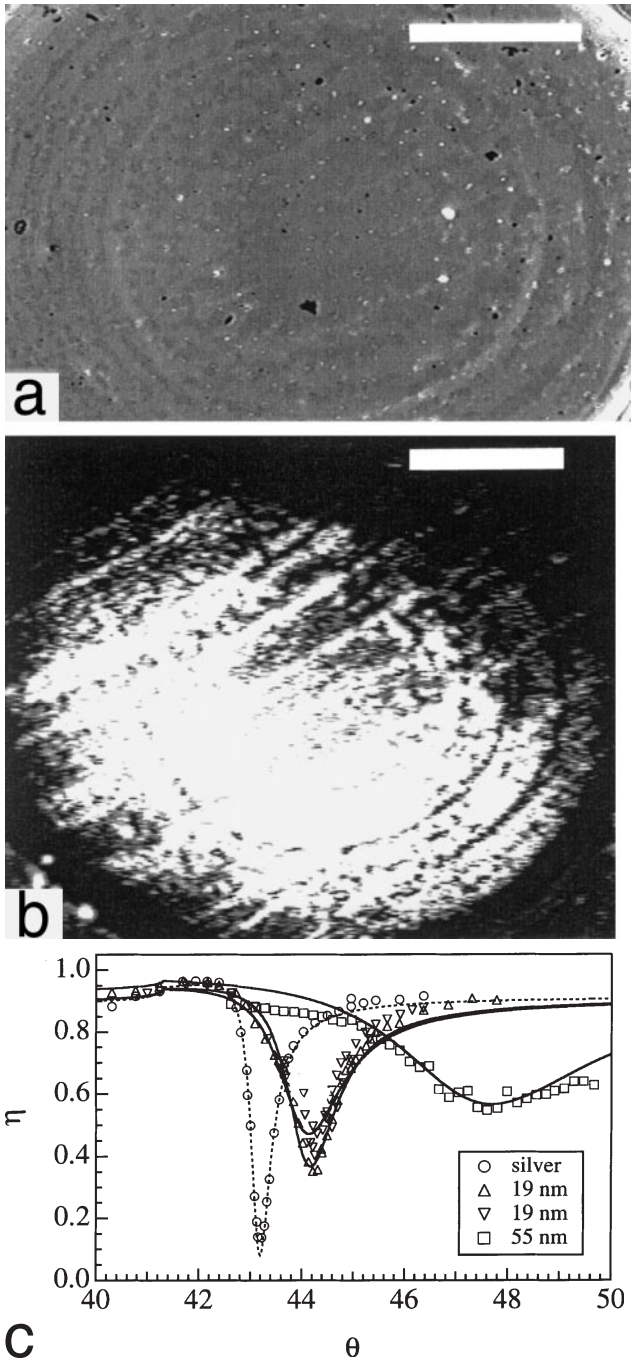

Fig. 18a–c Microscopic observations of nanometer particle layers deposited on a silver-coated glass plate. Photographs of a sample with a latex particle diameter of 19 nm (silver film thickness 55 nm, *bars* 0.5 mm): **a** Optical microscope image in reflected white light. **b** Corresponding surface plasmon resonance image in scattered light of wavelength 632.8 nm entering the silver film at an incidence angle of 44.25°, close to the reflectance minimum. **c** Angular dependence of the reflectivity of latex particle monolayers deposited on thin silver films. The theoretical curves are calculated [61] with the following values of optical parameters. For a particle diameter of 19 nm: first point $n = 1.177$, $k = 0.056$; second point $n = 1.163$, $k = 0.089$ ($d = 19$ nm). For a particle diameter of 55 nm: $n = 1.234$, $k = 0.057$ ($d = 55$ nm)

optical microscope, areas with different thickness (and refractive index) are distinguishable (Fig. 18b). They are of circular symmetry, resembling the growth-instability rings discussed previously, however, with no particle monolayer at the cell center. This is missing due to an unfavorable meniscus profile caused by increased wetting of the cell wall in the presence of added surfactant.

The monolayer of 55-nm particles is deposited on a silver film with parameters $d_{Ag} = 49.5\,nm$, $n_{Ag} = 0.061$ and $k_{Ag} = 3.951$, which determine a more-pronounced resonance minimum of η, not shown in Fig. 18c. The larger value of n for this latex is evidence for a denser particle monolayer.

Conclusion

Here we show that to grow 2D crystals of nanometer, submicron- and micron-sized particles on substrates, one should initially form a dense nucleus of well-ordered particles and of sufficient area. This resembles the crystallization from melts where, to initiate the crystallization, a crystal seed must be immersed in the molten material. In the 2D case the seed (nucleus) is created directly on the substrate, where the thickness of the suspension film becomes equal to the particle diameter. At that moment the latex particles are collected in ordered domains by the attractive capillary force. Once a 2D nucleus is formed, the crystal growth is mainly governed by the rate of evaporation and the meniscus profile. The convective water flow toward the ordered domain in the central region carries more particles to increase the overall crystal area with time. The competition between the particle transfer and the motion of the contact line leads to growth instability manifested as periodic concentric rings. The smaller the particles the larger the ring number and the number of layers in a ring. The latex layers are hexagonal crystalline lattices although square lattices are found locally being of intermediate thickness between two neighbouring layers.

Varying the evaporation rate (humidity) controls the crystallization rate. To obtain crystals of good structure one should maintain a high rate of crystallization, i.e. low humidity. The crystals of smaller particles grow faster than the crystals of larger particles. The best crystal structures are grown from a suspension of 0.001 volume fraction of particles. Both mica and glass seem suitable as substrates for 2D crystals.

Optical microscopy observation of the crystal structure and growth is possible even for submicron-sized latexes. For nanometer-sized particles, however, other methods such as SPR microscopy have to be applied.

Acknowledgements This research has been supported financially by the ERATO Program of the Research and Development Corporation of Japan (JRDC). The research was done as a collaboration between the Nagayama Protein Array Project of ERATO (C.D.D., H.Y., and K.N.) and the Laboratory of Thermodynamics and Physicochemical Hydrodynamics at the University of Sofia (C.D.D., G.S.L., and S.N.K.). The authors are thankful to P. Kralchevsky for the derivation of Eq. (1) and to T. Miwa for the AFM observations. C.D.D. is greatly indebted to Y. Yamaguchi from the Mitsubishi Chemical Corporation for encouragement and support in finalizing this work.

References

1. Kittel C (1978) Introduction to solid state physics. Wiley, New York pp 3, 8, 570
2. Gilliland GL (1988) J Cryst Growth 90:51
3. Nagayama K, Takeda S, Endo S, Yoshimura H (1995) Jpn J Appl Phys Part 1 34:3947
4. Bragg L, Nye JF (1947) Proc R Soc Lond Ser A 190:474
5. Bowden N, Terfort A, Carbeck J, Whitesides GM (1997) Science 276:233
6. Arora AK, Tata BVR (eds) (1996) Ordering and phase transitions in charged colloids. VCH, New York
7. Hiltner PA, Krieger IM (1969) J Phys Chem 73:2386
8. Hachisu S, Kobayashi Y, Kose A (1973) J Colloid Interface Sci 42:342
9. Kose A, Ozaki M, Takano K, Kobayashi Y, Hachisu S (1973) J Colloid Interface Sci 44:330
10. Williams R, Crandall RS (1974) Phys Lett A 48:225
11. Takano K, Hachisu S (1977) J Chem Phys 67:2604
12. Clark NA, Hurd AJ, Ackerson BJ (1979) Nature 281:57
13. Goodwin JW, Ottewill RH, Parentich A (1980) J Phys Chem 84:1580
14. Daly JG, Hastings R (1981) J Phys Chem 85:294
15. Ise N, Okubo T, Sugimura M, Ito K, Nolte HJ (1983) J Chem Phys 78:536
16. Furusawa K, Tomotsu N (1983) J Colloid Interface Sci 93:504
17. Aastuen DJW, Clark NA, Cotter LK, Ackerson BJ (1986) Phys Rev Lett 57:1733
18. Okubo T (1990) J Chem Soc Faraday Trans 86:2871
19. Yoshida H, Ito K, Ise N (1991) J Chem Soc Faraday Trans 87:371
20. Pieranski P, Strzelecki L, Pansu B (1983) Phys Rev Lett 50:900
21. Van Winkle DH, Murray CA (1986) Phys Rev A 34:562
22. Murray CA, Van Winkle DH (1987) Phys Rev Lett 58:1200
23. Chowdhury A, Ackerson BJ, Clark NA (1985) Phys Rev Lett 55:833
24. Burns MM, Fournier JM, Golovchenko JA (1989) Phys Rev Lett 63:1233
25. Burns MM, Fournier JM, Golovchenko JA (1990) Science 249:749
26. Pieranski P (1980) Phys Rev Lett 45:569
27. Onoda GY (1985) Phys Rev Lett 55:226
28. Lazarov GS, Denkov ND, Velev OD, Kralchevsky PA, Nagayama K (1994) J Chem Soc Faraday Trans 90:2077
29. Velev OD, Furusawa K, Nagayama K (1996) Langmuir 12:2374
30. Alfrey TA, Bradford EB, Vanderhoff JW, Oster G (1954) J Opt Soc Am 44:603
31. Kubitschek HE (1961) Nature 192:1148
32. Luck W, Klier M, Wesslau H (1963) Naturwissenschaften 14:485
33. Krieger IM, O'Neill FM (1968) J Am Chem Soc 90:3114
34. Gerould CH (1950) J Appl Phys 21:183
35. Davidson JA, Collins EA (1972) J Colloid Interface Sci 40:437

36. Wang Y, Juhue D, Winnink MA, Leung OM, Goh MC (1992) Langmuir 8:760
37. Deckman HW, Dunsmuir JH (1982) Appl Phys Lett 41:377
38. Deckman HW, Dunsmuir JH (1983) J Vac Sci Technol B 1:1109
39. Deckman HW, Dunsmuir JH, Garoff S, McHenry JA, Peiffer DG (1988) J Vac Sci Technol B 6:333
40. Hayashi S, Kumamoto Y, Suzuki T, Hirai T (1991) J Colloid Interface Sci 144:538
41. Burmeister F, Shafle C, Matthes T, Bohmish M, Boneberg J, Leiderer B (1997) Langmuir 13:2983
42. Chevreau A, Phillips B, Higgins BG, Risbud SH (1996) J Mater Chem 6:1643
43. Velev OD, Jede TA, Lobo RF, Lenhoff AM (1997) Nature 389:447
44. Matsushita S, Miwa T, Fujishima A (1997) Langmuir 13:2582
45. Rehg TJ, Higgins BG (1992) AIChE J 38:489
46. Denkov ND, Velev OD, Kralchevsky PA, Ivanov IB, Yoshimura H, Nagayama K (1993) Nature 361:26
47. Denkov ND, Velev OD, Kralchevsky PA, Ivanov IB, Yoshimura H, Nagayama K (1992) Langmuir 8:3183
48. Dushkin CD, Yoshimura H, Nagayama K (1993) Chem Phys Lett 204:455
49. Dimitrov AS, Dushkin CD, Yoshimura H, Nagayama K (1994) Langmuir 10:432
50. Yamaki M, Matsubara K, Nagayama K (1993) Langmuir 9:3154
51. Dimitrov AS, Yamaki M, Nagayama K (1995) Langmuir 11:2682
52. Kralchevsky PA, Paunov VN, Ivanov IB, Nagayama K (1991) J Colloid Interface Sci 151:79
53. Kralchevsky PA, Paunov VN, Denkov ND, Ivanov IB, Nagayama K (1993) J Colloid Interface Sci 155:420
54. Kralchevsky PA, Nagayama K (1994) Langmuir 10:23
55. Dushkin CD, Kralchevsky PA, Yoshimura H, Nagayama K (1995) Phys Rev Lett 19:3454
56. Dimitrov AS, Nagayama K (1996) Langmuir 12:1303
57. Adachi E, Nagayama K (1996) Langmuir 12:1836
58. Picard G, Nevernov I, Alliata D, Pazdernik L (1997) Langmuir 13:264
59. Picard G (1997) Langmuir 13:3226
60. Dushkin C, Miwa T, Nagayama K (1998) Chem Phys Lett 285:259
61. Kotsev S (1994) Diploma. University of Sofia
62. Dushkin CD, Nagayama K, Miwa T, Kralchevsky PA (1993) Langmuir 9:3695
63. Koschmieder EL, Pallas SG (1974) Int J Heat Mass Transfer 17:991
64. Adachi E, Dimitrov AS, Nagayama K (1995) Langmuir 11:1057
65. Adachi E, Dimitrov AS, Nagayama K (1996) ACS Symp Ser 648:418
66. Maenosono S, Saita S, Dushkin CD, Yamaguchi Y, Nagayama K, Tsuji Y (1998) Proc Int Coating Sci Technol Symp Newark Delaware, Univ Delaware, p 247
67. Raether H (1988) Surface plasmons on smooth and rough surfaces and on gratings. Springer, Berlin Heidelberg New York